

Electron microscopy investigations of microstructural alterations due to classical Rolling Contact Fatigue (RCF) in martensitic AISI 52100 bearing steel



Viktorija Šmelova ^{a,b,*}, Alexander Schwedt ^b, Ling Wang ^a, Walter Holweger ^{a,c}, Joachim Mayer ^b

^a National Centre for Advanced Tribology at Southampton (nCATS), University of Southampton, University Road, Southampton SO17 1BJ, UK

^b Central Facility for Electron Microscopy (GFE), RWTH Aachen University, Ahornstraße 55, 52074 Aachen, Germany

^c Schaeffler Technologies AG & Co. KG, Industriestraße 1–3, 91074 Herzogenaurach, Germany

ARTICLE INFO

Article history:

Received 17 October 2016

Received in revised form 21 January 2017

Accepted 23 January 2017

Available online 24 January 2017

Keywords:

Steel

Martensite

Rolling Contact Fatigue (RCF)

Electron microscopy

ABSTRACT

Substantial microstructural changes have been found to occur in bearing steels when subjected to high stress Rolling Contact Fatigue (RCF) and have been mainly reported in literature between the 1940s and 1990s. However, owing to limitations in the characterisation techniques available at the time, inconsistent interpretation and use of discrepant terminology have caused considerable difficulties in defining the microstructural changes accurately and unambiguously. In the present work, we have investigated the typical microstructural alterations, including Dark Etching Region (DER), Low Angle Bands (LABs) and High Angle Bands (HABs), and their formation mechanisms in RCF failed AISI 52100 (100Cr6) bearing steels using a combination of advanced microstructure characterisation techniques, including Scanning Electron Microscopy (SEM), Electron Backscatter Diffraction (EBSD) coupled with Energy Dispersive X-ray Spectroscopy (EDX), Transmission Electron Microscopy (TEM), and nanohardness measurements. Based on this combined approach, we are now able to give detailed insight in the plasticity-induced transformation and degradation mechanisms during high-stress RCF. The results show that new globular and elongated grains with distinct textures form during all stages of RCF, however a redistribution of chemical elements was only observed during the later stages of RCF. This has provided a significant insight in the formation mechanisms of DER, LABs and HABs. A model of the sequence of microstructure alterations during RCF is thus been proposed based on the findings.

© 2017 Published by Elsevier Ltd.

1. Introduction

Materials in rolling element bearings are stressed during cyclic loading resulting in the formation of irreversible subsurface microstructural alterations such as Dark Etching Region (DER) and White Etching Bands (WEBs), which had been reported frequently in literature between the 1940s and 1990s in bearing steels, such as through-hardened martensitic AISI 52100 steel. The terminologies of DER and WEBs was derived from the microstructure features in bearing steels that appear to be “dark” and “white” respectively after being Nital or Picral etched and observed under Light Optical Microscopy (LOM).

DER was firstly observed in bearing inner races below wear track by Jones in 1946 [1]. Similar features were also reported by

others with different names such as dark tint or needle [2], Dark Etching Constitution (DEC) [3,4], low temperature bainite [5], ferrite [6–8] and mechanical troostite [1] or tempered martensite [9,10]. DER has been reported to typically form under moderate to high contact stresses in the area of maximum shear stress after a high number of rolling cycles (5–100 million cycles) [5,9,11–16]. DER has also been typically found at a depth of approximately 0.10–0.65 mm below the contact surface [9,12,17]. DER typically spans between 0.5 and 2 mm in the depth direction, it however increases with running time and contact pressure [1,9,18]. There is no clear boundary between DER and the unaltered steel matrix, i.e. the change is gradual.

The dark contrast observed in DER under LOM was subsequently found to be randomly scattered deformed elongated patches under high magnification imaging due to stronger etchant concentration [5,9,19]. These dark etched patches have been reported to be a mixture of martensite and ferrite [2,5,9,12]. It was suggested that the dark appearance after etching was due to

* Corresponding author at: National Centre for Advanced Tribology at Southampton (nCATS), University of Southampton, University Road, Southampton SO17 1BJ, UK.

E-mail address: v.smelova@soton.ac.uk (V. Šmelova).

the slip motion in the lattice [20,21]. The dislocation density within DER has generally been found to be high [5,12], however it was also found reduced in many cells [12]. Voskamp [16] suggested that carbon migration from martensite to heavily dislocated regions resulted in the formation of DER. Martin et al. [7] concluded that improvements in steel making over the years had resulted in the elimination of DER formation since no DER formed in their study. Others also suggested that DER was just an effect of the over-tempering of martensite since no DER was observed in the steel being tempered to a hardness of 57 HRC [18,22].

WEBs have been found to form at a later stage during RCF testing typically within DER but have also been found to form without DER formation. WEBs are parallel three-dimensional thin plates that appear to be parallel to the contact surface in the axial cross-section (perpendicular to the rolling direction), inclined to the surface in the circumferential cross-section (parallel to the rolling direction), and broadened in their own plane [5–7,14,16,21,23]. WEBs are a combination of bands that rise towards the surface in the rolling direction [23,24] at an angle of either 30° (ranging from 20 to 35°) or 80° (ranging from 65 to 85°), thus are named Low Angle Bands (LABs) and High Angle Bands (HABs) respectively [7]. The angles of the bands were found to vary with the bearing type, e.g. ball or cylindrical roller bearings, within the ranges mentioned above [7,13], however no details on how they were related were provided by the researchers. WEBs mainly form in highly stressed zones and the density of WEBs increases with the rolling cycles [7]. LABs start to form after about 100 million cycles followed by HABs that occur after about 500 million cycles [9]. However Mitamura et al. found HABs formed before LABs under high contact pressure of 4.6 GPa and 5.5 GPa [4].

LABs have been described as disc-shaped regions of ferrite bordered by unusual narrow elongated features that were not broken during tempering [7,8] thus had been referred to as lenticular carbides [6,7]. LABs have been reported as 5–30 μm long, 0.1–0.5 μm thick bands with 0.5–10 μm spacing between them [5,9]. Thicker bands (up to 2 μm thickness) have also been reported [16,18].

HABs are longer, thicker bands compared to LABs [9,16,17,21,23]. They are typically about 100 μm long, 10 μm thick and the spacing between the bands varies from 5 to 50 μm [9]. Swahn et al. [9] were able to show from their TEM analysis that HABs consist of heavily deformed ferrite with about 0.2 μm cell size.

Beswick et al. [25] were the first and only group who found a crystallographic {111}{112} texture had developed in regions of the altered microstructure using the X-ray pole figure technique and the analysis of diffraction intensity maximum variation with depth. Their results suggested that this texture was formed by dynamic recrystallisation. Unfortunately no further analysis has been performed to confirm. However these findings have been considered paradoxical and thus ignored by others [24].

Martin et al. [7] showed both WEBs and lenticular carbides in a LOM image of a bearing race in Nital etched condition, where WEBs appeared white while lenticular carbides were dark and thin. However, Swahn et al. [9] and Osterlund et al. [5] claimed that the white parts are lenticular carbides and the dark thin structures are ferrite based on their TEM results.

Lenticular carbides attached to LABs have been proposed to be formed by plastic deformation (flattening) of the primary spheroidised carbides [18]; or due to carbide dissolution in the LAB and precipitation at the edge of the LAB in the form of lenticular carbides [8,26]. Zwirlein [20] and Swahn et al. [9] suggested that LABs consist of ferrite particles surrounded by carbon-rich (carbide-like) zones. Martin et al. [7] and Osterlund et al. [5] also showed in their TEM and electron diffraction patterns analyses that LABs are very fine ferrite grains.

LABs are often seen to be extended into primary spheroidised carbides that eventually break up [9,27]. Intact primary spheroidised and/or tempered carbides are generally not observed in well-developed LABs and HABs [6,7,27]. However, Martin et al. [7] suggested that the primary spheroidised carbides always existed in the LABs and the reason for not being observed after etching was due to the relatively higher etch resistance of the bands. Carbide breaks-up during LAB/HAB formation have been suggested to be thermally induced [26,27], as temperature increase plays an important factor in the microstructural changes [2,16]. A temperature increase of 100–200 °C above the operating temperature due to localized plastic deformation was also suggested to be required for LAB formation [26]. Nevertheless, Swahn et al. [27] believed that thermal activation could not be the only cause of the break-up process however no other suggestions were given.

Muroga et al. [28] found that the concentration of carbon in the steel matrix and the DER was nearly the same, whereas it dropped to 0.2 wt% and 0 wt% in LABs and HABs respectively, which was similar to the 0.06 wt.% (very low) [17] and zero [9] carbon content in HABs found by others.

The hardness of DER has generally been found to be similar to that of the surrounding matrix. An increase in the hardness of DER was also reported [2], which was considered to be associated with the work hardening of martensite or the transformation of retained austenite to martensite [2,23]. Others also reported a lower hardness in DER [1,2,9,12,22,29], which was thought to be related to the start of WEBs formation since WEB has been reported to have a lower hardness than the matrix due to its lower carbon content [20]. The hardness measurements presented in literature are in general lacking of details and are causing confusions. Further systematic hardness analysis is therefore desirable.

Many studies have been conducted to develop analytical/numerical models for the formation and orientation of WEBs [2,16,21]. Prior to the 1990s, most of the studies only considered maximum shear and principal stresses, or maximum plastic principal strain in their models for the formation of WEBs. This was based on the fact that WEBs are typically seen around the area of maximum shear stress. Moreover, 2.5 GPa was reported as the lowest threshold for the microstructural alterations, suggesting its relationship with plastic deformation. Modelling to correlate microstructural alterations with carbon diffusion was attempted by Polonsky and Keer [24], however the problem stays unresolved due to unclarified limitations in their models.

Despite the amount of efforts given to this topic over the past few decades, there is a strong need for a systematic study of DER, LABs and HABs to clarify and define the terminologies and their distinct microstructures, hardness and formation mechanisms. While carbides and carbon movement are believed to play a key role in the formation and development of microstructural alterations during RCF, the role of stresses and the definitive mechanisms for the low and high angle bands remain unclear. By using a combination of modern material characterisation techniques, including EBSD combined with EDX and Backscattered Electron (BSE) imaging in SEM, TEM and nanohardness analysis, this paper presents the results from a comprehensive analysis of DER, LABs and HABs in AISI 52100 bearing steel produced from classical fatigue tests to provide an insight to these RCF phenomena.

2. Experimental details

2.1. Material

All specimens examined in this study were cut from bearings made of the standard through-hardened AISI 52100 (also known as 100Cr6) bearing steel that had been subjected to a standard heat

treatment process including austenitisation at 830–860 °C and quenched in oil to 60 °C followed by tempering at 170–220 °C for 2 h. The chemical composition of the specimens, measured by the Sheffield Assay Office using an inductively coupled plasma optical emission spectrometry, is given in **Table 1**. The elements carbon and sulphur were determined using combustion analysis. AISI 52100 bearing steel has a typical microstructure consisting of tempered martensite with homogeneously distributed primary spheroidised carbides $(\text{Fe,Cr})_3\text{C}$, tempered carbides and approximately 10–12% retained austenite. **Fig. 1** shows the SE and BSE SEM images of the AISI 52100 (100Cr6) bearing steel microstructure taken from an unaltered region of the ball specimens (introduced below), where the red arrows point to the spheroidised carbides in both modes. Tempered carbides were not detected in these images as they typically appear as fine cementite (Fe_3C) particles at grain boundaries, or inside martensite or bainite structures and due to their small size and the fact that the study presented in this paper has been primarily performed by use of scanning electron microscopy (SEM, EBSD, EDX) such tempered carbides could not be observed at this scale and hence it is difficult to discuss their degradation.

2.2. Fatigue testing

The specimens examined in this study were cut from two ball bearings subjected to RCF testing after the structural transformations of DER, LABs and HABs had occurred.

The DER specimen was cut from a ball in a grease lubricated double row angular contact ball bearing after being tested on an industry standard RCF test rig L24. During the test, the bearing rotating speed varied from 800 to 2000 rpm while the contact pressure was kept at 5287 MPa (max). The test was terminated at 244 h (approximately 11.7–29 million cycles) when one of the balls failed with a surface spall. The ball that the specimen was cut from has no spall.

The LAB/HAB specimen was cut from the inner ring of an angular contact ball bearing of 7205B type after being tested on an industry standard RCF test rig L17. During the test, the bearing rotating speed was kept at 12,000 rpm and the maximum contact pressure at 2900 MPa. The bearing was lubricated with ISO VG 68 oil and the temperature of the lubricant was maintained at 80 °C. The test was terminated at 549 h (approximately 400 million cycles) when the bearing failed with pitting.

2.3. Microstructural characterisation methodology

All specimens were mechanically polished starting with 3 µm, followed by 1 µm and 0.25 µm diamond suspensions. Colloidal silica suspension (OP-S) was used as the final preparation step to achieve the necessary deformation-free surface for obtaining orientation contrasts in BSE images in SEM and EBSD analyses. BSE imaging is applied under conditions favourable for showing orientation contrasts in the images, also known as Electron Channelling Contrast Imaging (ECCI) or orientation contrast imaging. After BSE and EBSD analyses specimens were slightly re-polished to remove the contamination layer and etched with 1% Nital solution (1 ml HNO_3 , 99 ml Ethanol) for 1–3 s for imaging with LOM (Olympus BX51) and Secondary Electrons (SE) in the SEM, a JEOL JSM

7000F field emission gun microscope equipped with a combined EDAX Pegasus EDX/EBSD system.

The BSE and SE SEM investigations were performed at an accelerating voltage of 10 kV with approximately 5 mm and 10 mm Working Distance (WD), respectively. EBSD investigations were performed at an accelerating voltage of 15 kV and probe current of 30–35 nA under WD of 15–17 mm with varying step sizes, such as 25 nm and 50 nm.

The EBSD data were evaluated with EDAX OIM 7.3 without additional data clean-up applied. For indexing purposes the phases of α -Fe, γ -Fe and Fe_3C were chosen.

Transmission Electron Microscopy (TEM) analysis was conducted on specimens prepared using a Focused Ion Beam (FIB) work station FEI Strata 205. Tungsten layer deposition was used for surface protection. Milling was performed at an acceleration voltage of 30 kV with different currents starting with 20.2 nA and finishing off with 3.49 pA. The cut lamella was placed onto a Cu grid for imaging. TEM Bright Field (BF) and Dark Field (DF) images, as well as Selected Area Electron Diffraction Patterns (SADP) were obtained using an FEI Tecnai F20, operating at 200 kV.

2.4. Nanohardness analysis

Nanohardness measurements were performed on DER, LAB and HAB features in Nital etched condition using a Berkovich tip on the nanoindentation system (Micro Materials, NanoTest Vantage). Nanoindentation mapping tests were carried out in depth control mode by applying a maximum depth of 300 nm. In accordance to BS EN ISO 14577-1:2015 standards, the arithmetic mean deviation of the surface roughness should be no more than 5% of the minimum penetration depth to ensure that the surface roughness has no effect on the hardness mapping. The slightly etched surface was checked using a Taylor-Hobson Talysurf 120L profilometer to ensure that its arithmetic mean deviation surface roughness was kept within 10 nm and thus etching was used for easier identification of the areas of interest. Fixed 2 mN/s loading/unloading rates and 20 s dwell time at maximum load were used for all nanohardness measurements in this study. Thermal drift correction data were collected for 30 s before and after the indentation test. After nanohardness analysis all the indents were checked under SE SEM (JEOL, JSM-6500F) to confirm the areas of indentation. The average of at least 3 indent measurements was used as the hardness value for each feature.

3. Results

3.1. Dark Etching Region (DER)

An LOM image of the DER in the subsurface of the ball specimen is shown in **Fig. 2(a)** (marked between the two white broken lines). It can be seen that the DER extends from approximately 80–600 µm below the contact surface. **Fig. 2(b)** shows an enlarged area of the DER, where a combination of small black patches intermixed with bright areas and small white primary spheroidised carbides are observed. Further observation of the DER under SEM shows that the primary spheroidised carbides appear to be smooth and flat protrusions in SE SEM, but dark spherical areas in BSE SEM,

Table 1
Chemical composition of the two studied specimens, wt%.

	C	Cr	Si	Cu	Mn	Al	P	Co	Zn	S	Sn	Ni	Mo
DER	1.55	1.47	0.21	0.01	0.39	0.01	<0.01	<0.01	<0.01	<0.003	<0.01	<0.01	<0.01
LAB/HAB	0.95	1.51	0.27	0.11	0.42	<0.01	<0.01	<0.01	<0.01	0.005	<0.01	0.03	<0.01

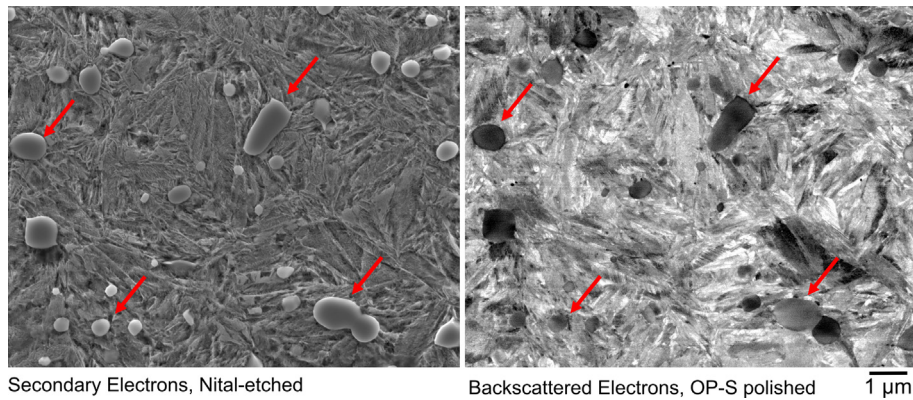


Fig. 1. SE and BSE SEM images of the virgin through-hardened martensite AISI 52100 (100Cr6). Red arrows showing examples of primary spheroidised carbides $(\text{Fe,Cr})_3\text{C}$.

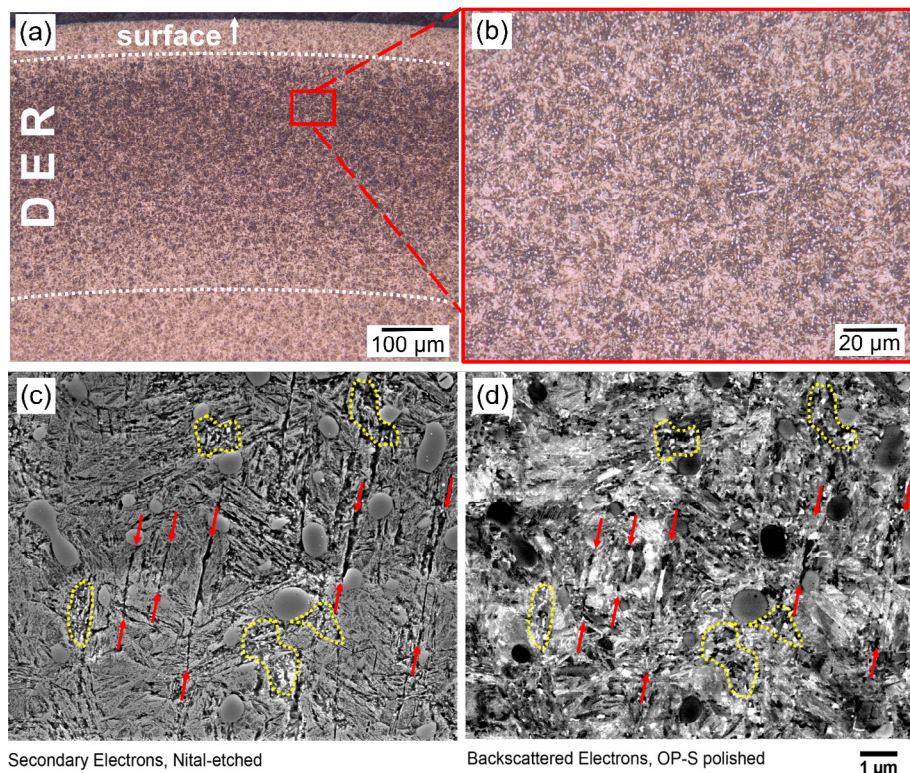


Fig. 2. Images of DER: (a), (b) viewed with LOM (Nital etched), (c) viewed with SE SEM (Nital etched); and (d) viewed with BSE SEM (OP-S polished). Elongated and globular grains are marked with red and yellow, respectively.

see Fig. 2(c) and (d). The dark patches observed under LOM are found to be correlated with the clusters of elongated dark features appearing as deep grooves (marked with red arrows) under SE SEM (Nital etched) shown in Fig. 2(c), but with clusters of elongated grains (marked with red arrows) under BSE SEM (OP-S polished) shown in Fig. 2(d). In addition to the elongated grains, groups of small globular grains are observed in both SEM images due to a slightly stronger attack of the etchant at these sites, see examples of these are marked with yellow circles in Fig. 2(c) and (d).

The DER was also examined using a combined EBSD/EDX measurement and the results are shown in Fig. 3, where Fig. 3(a) shows an EBSD map of austenite and $(\text{Fe,Cr})_3\text{C}$ carbides covering an area from the surface to a depth of 200 μm below the surface, and Fig. 3(b) shows the corresponding EDX maps of carbon (C-K α) and chromium (Cr-K α) in this area. It can be seen that the amount of retained austenite in the DER is much lower than that in the

unaffected area while the distribution of primary spheroidised carbides remains homogeneous and unchanged in the DER compared with that in the unaffected area (see in Fig. 3(a)).

The EDX analyses show a high concentration of carbon and chromium in the primary spheroidised carbides and a homogeneous distribution of carbon in the matrix, see Fig. 3(b). A slightly inhomogeneous chromium distribution in the matrix is also observed, where chromium-depleted regions appear around clusters of primary spheroidised carbides in the matrix. However, both carbon and chromium distributions in DER are same as that in the typical AISI 52100 bearing steel microstructure.

Both the martensitic matrix and the altered microstructure components in DER have been indexed as α -Fe, i.e. Body Centred Cubic (BCC), by EBSD. However, a Kernel Average Misorientation (KAM) map, which depicts the average grain-internal orientation change of the crystal lattice over a distance of 100 nm, shows

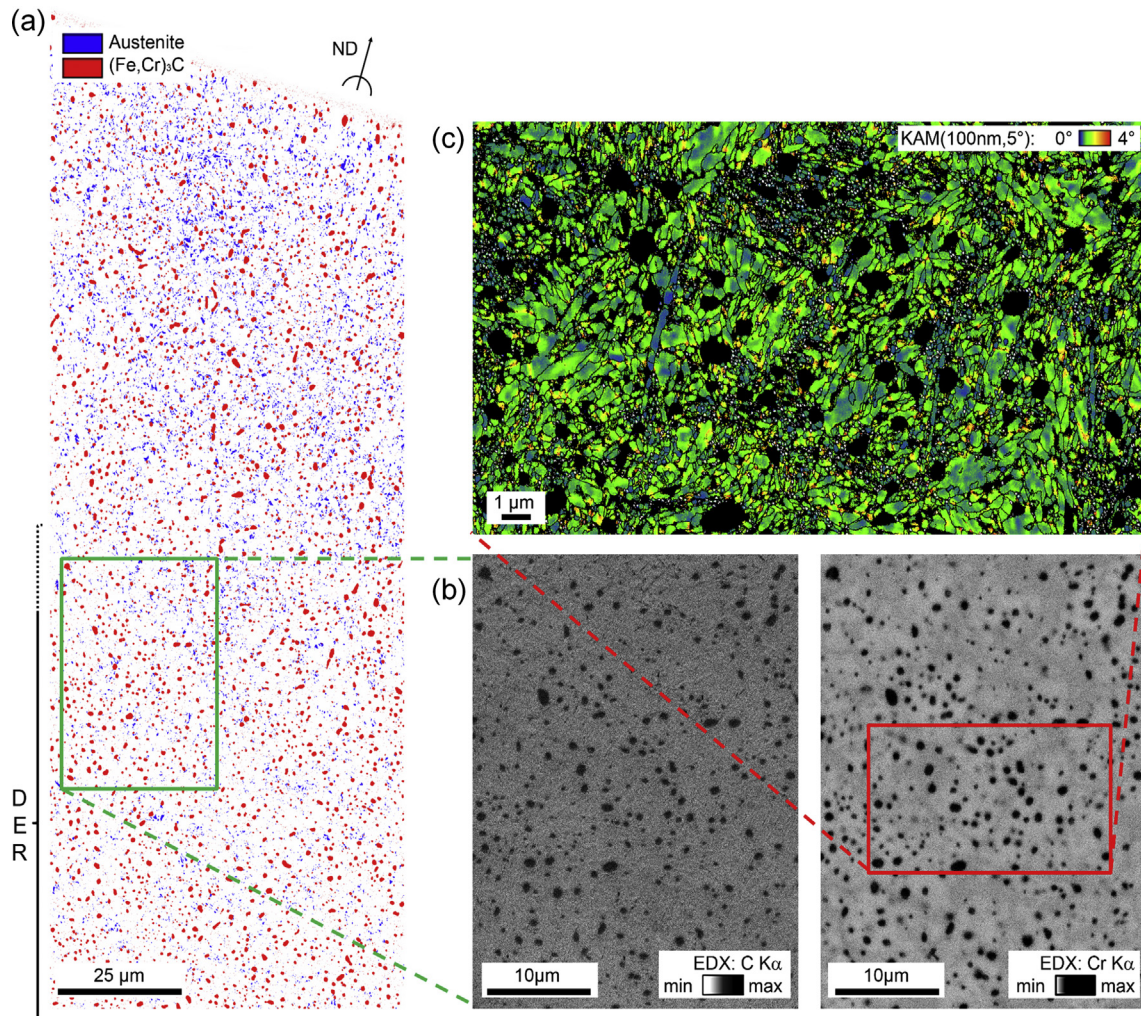


Fig. 3. Maps of the DER: (a) An EBSD map of austenite and $(\text{Fe},\text{Cr})_3\text{C}$ carbides covering an area from the surface into depth of 200 μm below the surface. Step size 50 nm, Confidence Index (CI) > 0.1 ; (b) EDX maps of carbon (C-K α) and chromium (Cr-K α). Step size 25 nm, for the sake of visibility in the print, brightness and contrast corrections were applied on EDX maps resulting in the given greyscale flows; and (c) An EBSD KAM map of the points indexed as α -Fe with CI > 0.1 . Step size 25 nm.

slightly lower misorientation in the elongated and globular grains, see Fig. 3(c). Together with the fact that both elongated and globular grains are seen to be attacked more by Nital, it is suggested that globular and elongated grains are ferritic. In addition, comparing the KAM map with the chromium map, it seems that the small globular grains appear preferentially in the chromium-depleted regions mentioned above.

SE SEM micrographs of the nanoindents taken in an unaltered area between the surface and the DER as well as in an area with elongated and globular grains within the DER are shown in Fig. 4. The unaltered area has an average hardness of 10 GPa (Nano Berkovich hardness) while the DER with elongated and globular grains has approximately 7.5–7.9 GPa. Thus the DER has a slightly decreased hardness compared to the original steel matrix. The

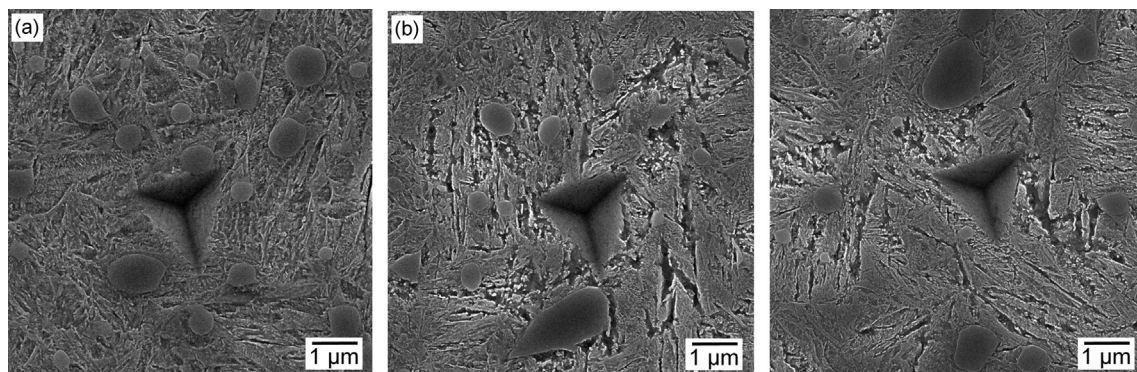


Fig. 4. SE SEM micrographs of nanoindents taken from specimen with DER: (a) unaltered area between surface and DER and (b) elongated and globular grains area.

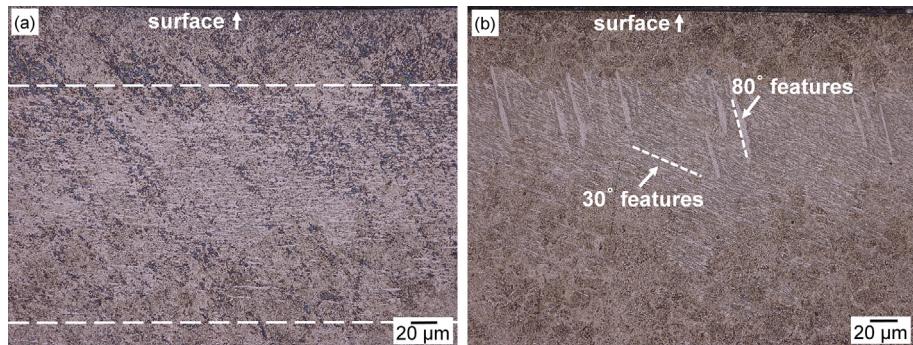


Fig. 5. LOM micrographs of 30° and 80° features in Nital etched condition: (a) in axial cross-section and (b) in circumferential cross-section.

extremely small features of the elongated and globular grains have inevitably caused difficulties in performing indents at exact locations even in this study. Furthermore, it is not possible to know how deep these grains extend.

3.2. 30° and 80° features

As shown in Fig. 5, the WEB features appear as parallel or inclined bands depending on the cross section orientation. Fig. 5 (a) and (b) shows LOM micrographs of the features in axial (perpendicular to the rolling direction) and circumferential (parallel to the rolling direction) cross-sections of a bearing race, respectively. During this study it also becomes evident that the WEBs are not homogeneous and consist of distinct features some of which are preferentially aligned at approximately 30° and others at approximately 80° with respect to the rolling direction in the circumferential cross-sections. Therefore, in the following discussions the terms "30° features" and "80° features" will be used instead of the general LABs and HABs terms.

Fig. 6 shows the altered microstructures comprising both 30° and 80° features viewed with SE SEM (Nital etched) in comparison with the EDX maps (OP-S polished) of the same region. It can be seen that the primary spheroidised carbides have been completely disintegrated in the altered regions. Chromium from the primary spheroidised carbides was homogenised in the 30° and 80° bands region (see Fig. 6(b)). Carbon appears to be homogeneously depleted in the 80° features giving lower X-ray intensities than in the martensitic parts of the unaltered matrix (see Fig. 6(c)). Similar carbon-depleted regions are seen intermixed with the carbon-rich areas among the 30° features showing two different forms of etching behaviour, a conchoidal surface structure mainly for the larger areas as well as long grooved structures (see Figs. 6 and 8). The carbon-rich components show a stronger resistance to Nital etching and appear similarly unaffected by etchant as the primary spheroidised carbides in the SE SEM image. A closer comparison between chromium and carbon EDX maps shows that, in contrast to the primary spheroidised carbides, the 30° and 80° structures are not chromium enriched.

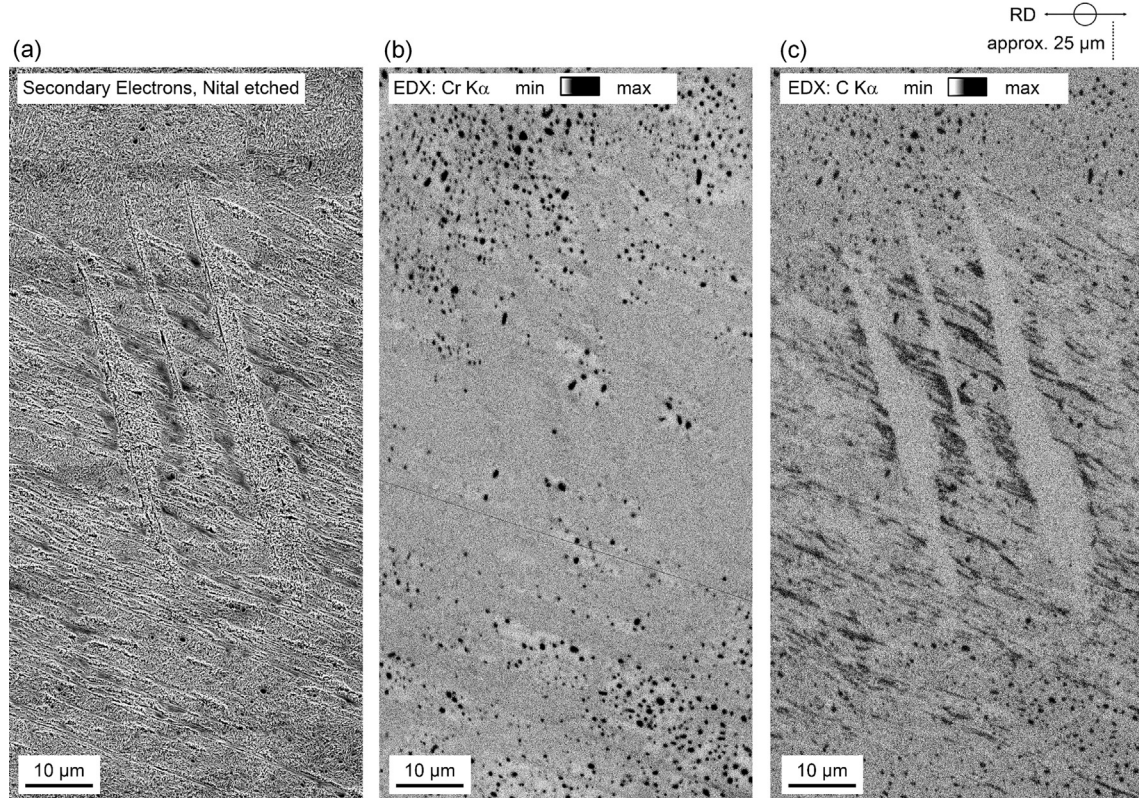


Fig. 6. A region showing 30° and 80° features: (a) SE SEM image (Nital etched); (b) EDX Chromium map (not etched); and (c) EDX Carbon map (not etched).

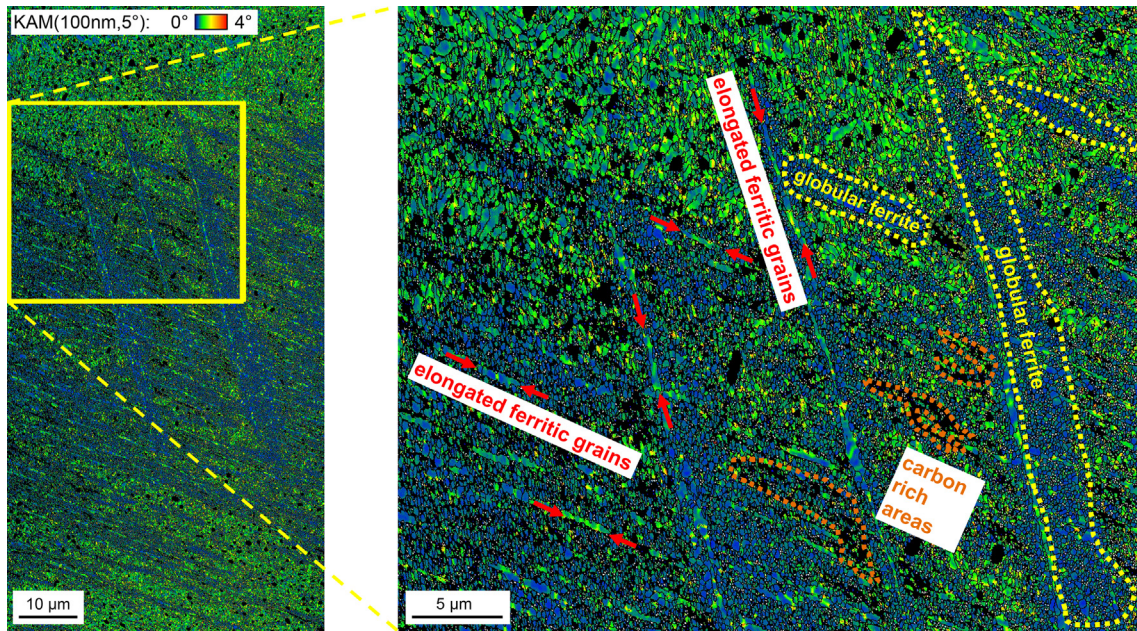


Fig. 7. A KAM map of the area in Fig. 6 for the points indexed as α -Fe with $CI > 0.1$. Step size 50 nm.

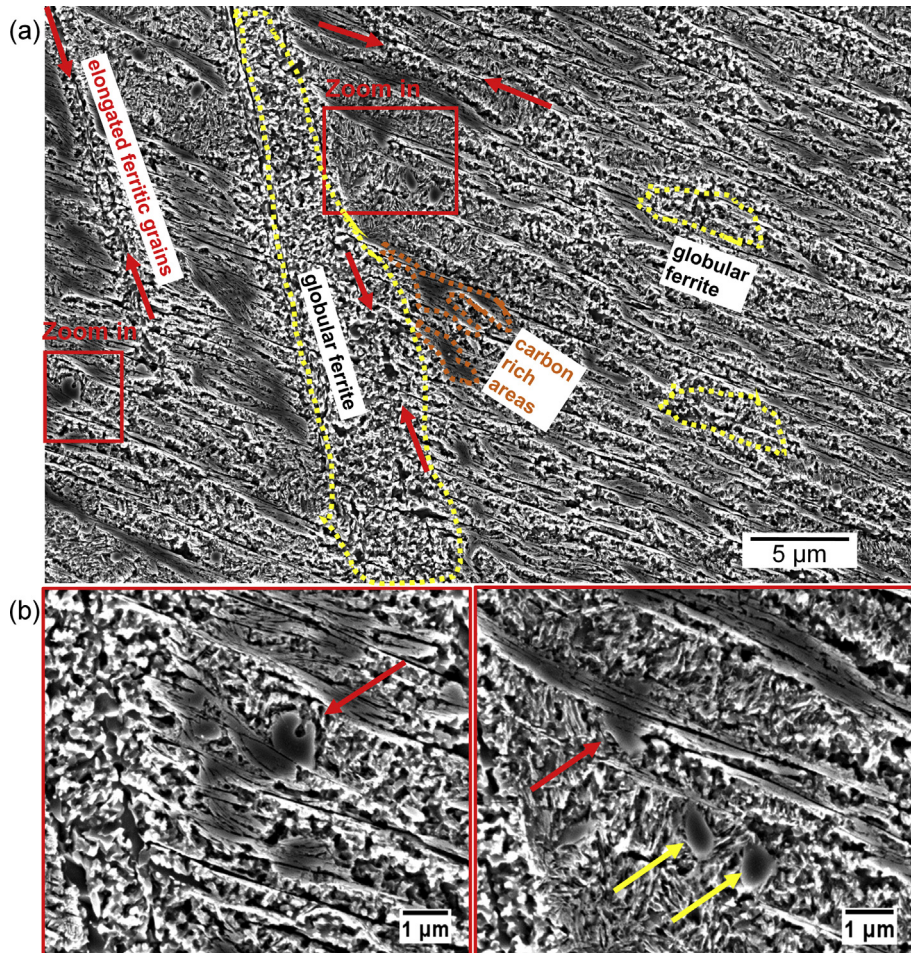


Fig. 8. High magnification SE SEM (Nital etched) micrographs of 30° and 80° features showing: (a) main constituents and (b) zoom in examples of the dissolving carbides (red arrows) and intact carbides (yellow arrows).

A KAM map of the features is shown in Fig. 7. It can be seen that large parts of the altered regions appear as equiaxed grains showing considerably lower misorientations than the initial matrix. Elongated grains with partly higher misorientations are also seen to be correlated to the elongated grooved structures in Fig. 6. Together with the comparatively high Image Quality (IQ) in the diffraction patterns and their etching behaviour, both components (equiaxed/globular and elongated grains) are considered to be ferritic.

Distinct regions marked in Fig. 7 are shown in a high magnification SE SEM image in Fig. 8(a), showing three different constituents in the 30° and 80° features, i.e. globular ferritic grains, elongated ferritic grains and carbon-rich areas. Breaking-up or dissolving primary spheroidised carbides are seen next to the carbon-rich areas (red arrows in Fig. 8(b)). Furthermore, intact primary spheroidised carbides are observed in the intermix area of the 30° features (Fig. 8(b) yellow arrows).

In order to further investigate the carbon-rich component in the altered region, TEM analysis has been performed on a FIB lamella that was cut across 30° features, see Fig. 9. The globular grains intermixed with lenticular structures are clearly seen in the dark field micrograph in Fig. 9(a). A high carbon content is observed in the lenticular structure (shown in Fig. 9(b)) that is in accordance with earlier analyses by SEM/EBSD/EDX. However the diffraction pattern of a carbon-rich area (Fig. 9(c)) is too complex to be unambiguously indexed, but nevertheless it is clearly observed that features are not nanocrystalline, more complex than a pure bcc or cementite pattern and could potentially be newly

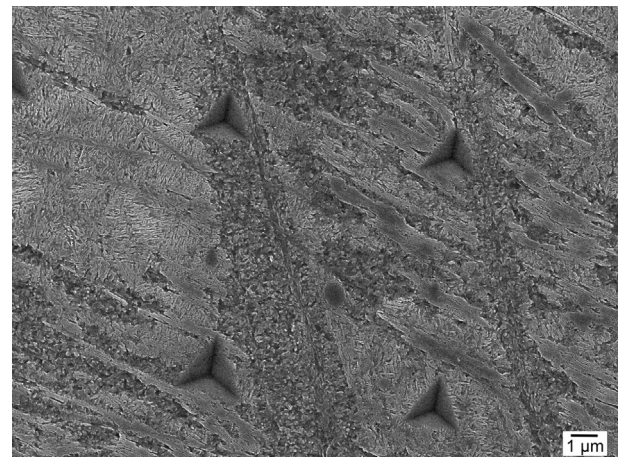


Fig. 10. An SE SEM image of the nanoindentations performed on the 30° and 80° features.

formed lenticular carbides with complex crystal structure, as suggested in [5–7,9].

Fig. 10 presents an SE SEM image of the nanoindentations performed on the 30° and 80° features. Nanohardness measurements were also performed on an unaltered region between the surface and the start of the altered region. The average hardness of the unaltered region is 7.76 GPa (Nano Berkovich hardness) and the globular ferritic grains and carbon-rich areas have an average hard-

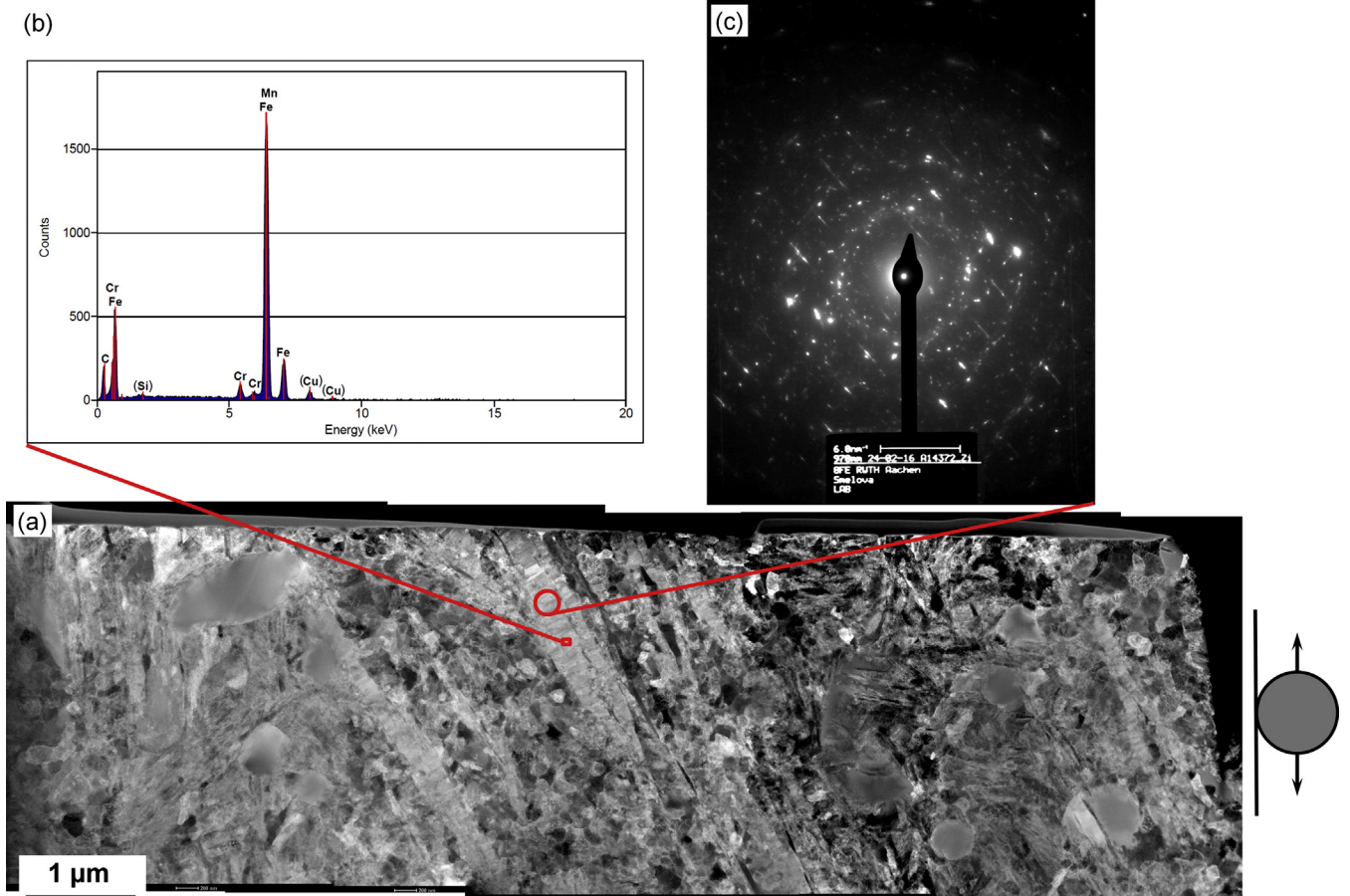


Fig. 9. TEM analysis of 30° features: (a) panorama of dark field images covering the entire FIB lamella showing carbon-rich areas and globular grains; (b) EDX spectrum on lenticular structures; and (c) SADP pattern on lenticular structure. The raceway is parallel to the right side of the image with rolling approximately in vertical direction.

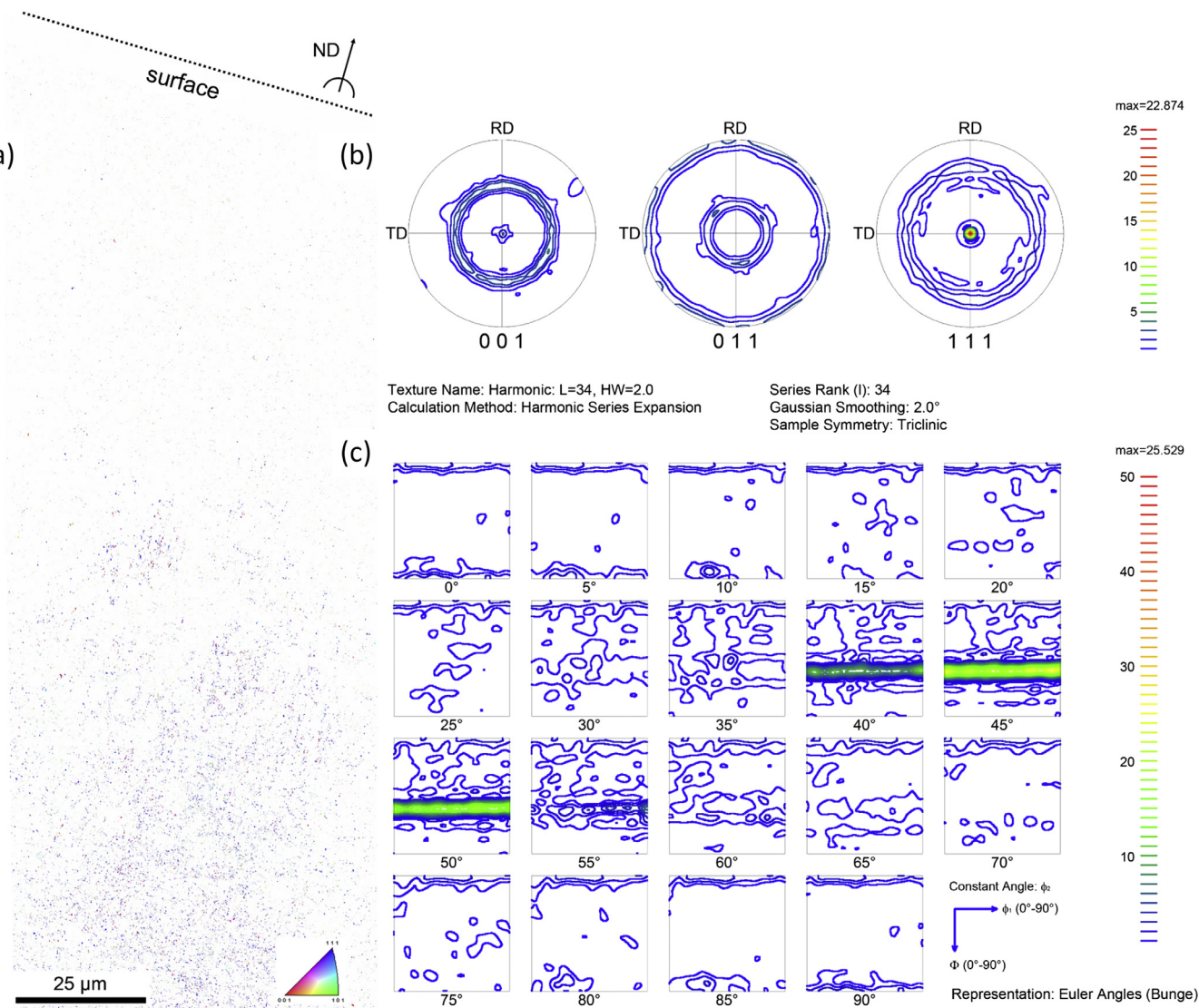


Fig. 11. Texture of the recrystallized grains during DER formation: (a) IPF with respect to the normal direction during rolling; (b) selected pole figures; and (c) orientation distribution function.

ness of 4.2–6 GPa and 9–11 GPa, respectively. Hence the hardness is found to be decreased in regions with globular ferritic grains but increased in regions with carbon-rich areas. These changes are thought to be resulted from the grain size variation, crystallography and chemical composition.

3.3. Texture analyses

To explore the formation mechanisms, texture analysis has been applied to the globular and elongated ferritic grains.

3.3.1. Dark Etching region (DER)

In order to understand the formation mechanisms of the globular and elongated ferritic grains in the DER, these newly formed grains were isolated by applying the following criterion in Orientation Imaging Microscopy (OIM) analysis:

DER components = α -Fe AND CI

> 0.1 AND grain orientation spread < 0.3°

This leads to a subset of data of approximately 100,000 points and approximately 17,000 newly formed grains. Since the resulting

grains were very small, a further subdivision into globular and elongated grains was not possible for the DER case, thus components were considered together.

An Inverse Pole Figure (IPF) map with respect to the local normal direction (ND) during rolling (see in Fig. 11(a)) is plotted for the selected grains. It is clearly visible that the density of these grains increases with the depth of the DER, which correlates with the earlier observations by SEM and EBSD. Further texture analysis by using pole figures (shown in Fig. 11(b)) indicates a rotational symmetry around the normal direction (ND). This is due to the fact that a ball specimen was used where the normal direction is the only fixed axis during rolling. The pole figures show that for most grains a $\langle 111 \rangle$ axis is aligned with the normal direction, for some other grains it is a $\langle 001 \rangle$ axis instead. This can also be clearly seen in the orientation distribution function shown in Fig. 10(c), where the orientations along the γ -fibre (i.e. the set of orientations with $\langle 111 \rangle$ axis parallel to the normal direction) show homogeneously high frequencies of about 25 times the frequency of a random orientation distribution. This γ -fibre orientation is a texture component often observed for recrystallisation components during the rolling of BCC-iron [30].

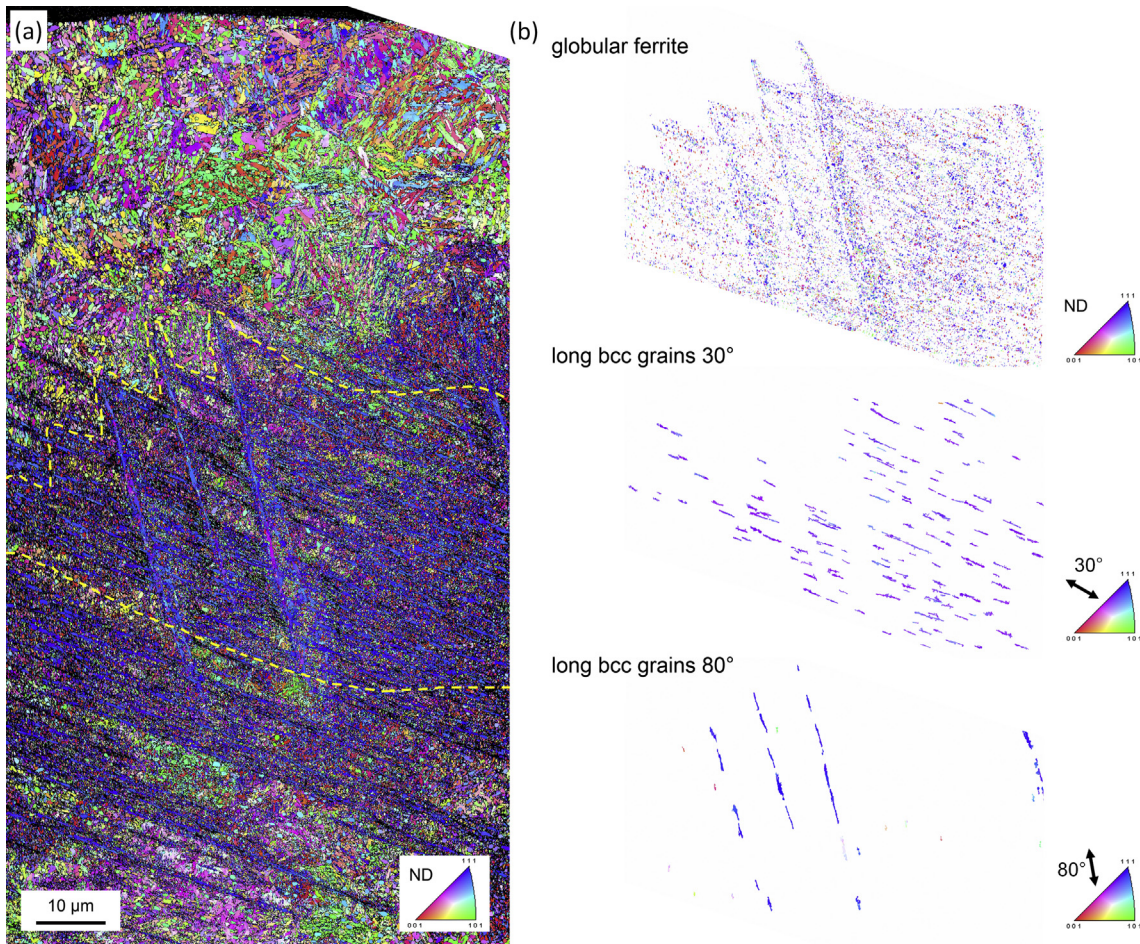


Fig. 12. IPF maps for the dataset from Figs. 4 and 7 that show: (a) point with respect to the local normal direction of the rolling for all points indexed as bcc with $CI > 0.1$; (b) selected alteration constituents from the region marked in yellow. The IPF map for the globular ferrite component is plotted with respect to the normal direction, the IPF maps for the elongated grains are plotted with respect to the 30° and 80° orientation of the features.

3.3.2. 30° and 80° features

In case of the 30° and 80° features, the newly formed components were isolated by applying the following criteria in OIM Analysis:

$$\text{Globular grains} = \alpha\text{-Fe AND } CI$$

$$> 0.1 \text{ AND grain orientation spread} < 0.26^\circ$$

$$\text{Elongated grains} = \alpha\text{-Fe AND } CI > 0.1 \text{ AND grain size}$$

$$> 0.4 \mu\text{m AND grain orientation spread}$$

$$> 1.5^\circ \text{ AND aspect ratio} < 0.25$$

Furthermore, the elongated grains were separated into 30° and 80° oriented grains via the shape orientation parameter.

The IPF map in Fig. 12(a) illustrates the change in texture of the whole altered region of 30° and 80° features compared to the initial base material, showing strong γ -fibre components, i.e. for a high number of grains a $\langle 111 \rangle$ axis is aligned with the rolling normal direction. Fig. 11(b) shows IPF maps for the elongated and globular grains separated. It is seen that the individual components have very homogeneous crystal orientations.

Further analysis by texture evaluation for the above defined components is shown in Fig. 13. For the globular ferritic grains, a mixture of orientations along the γ -fibre and the rotated cube orientation $\{001\} \langle 110 \rangle$ was found, which both are common texture

components during cold-rolling of BCC iron [30]. The pole figures projected to the plane spanned by rolling (RD) and normal direction (ND) for the elongated grains show that both 30° and 80° grains have a $\langle 111 \rangle$ direction close to the normal direction, thus the orientations are also close to the γ -fibre. Additionally, for both types of the elongated grains, a $\langle 111 \rangle$ direction as well as the trace of a $\{112\}$ plane are aligned with the shape orientation of the grains along the 30° and 80° orientation, respectively.

4. Discussion

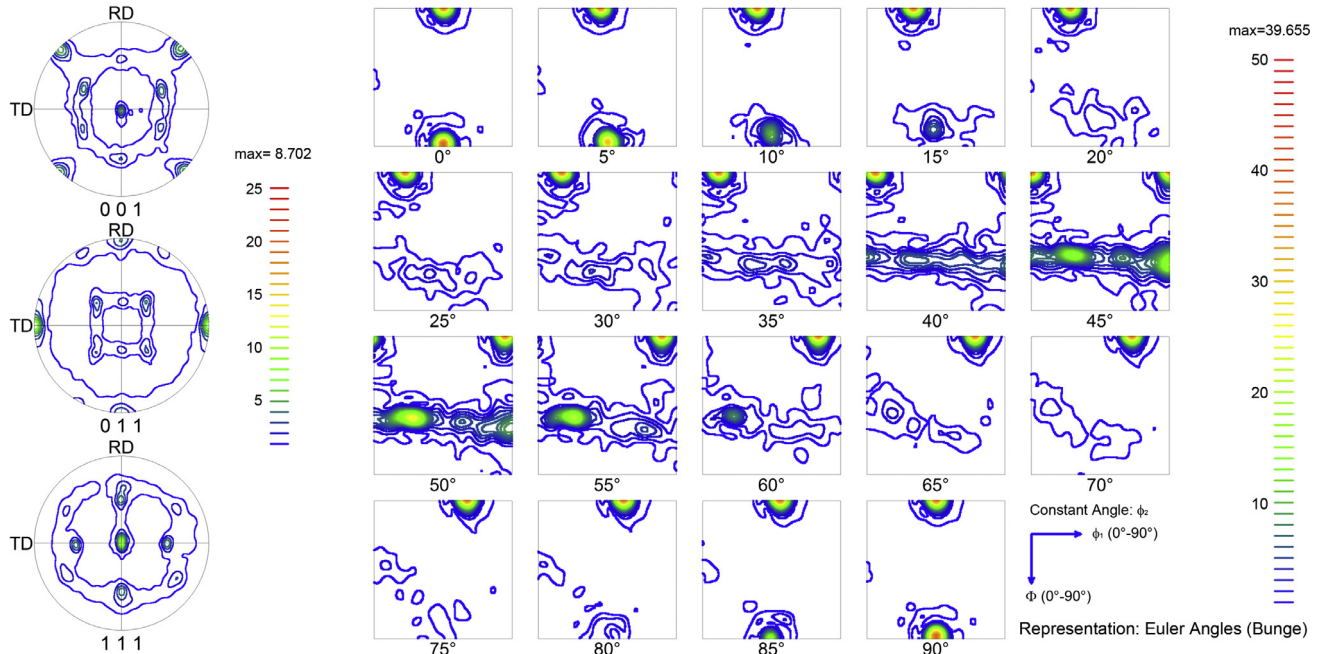
The sequence of the microstructure alterations taking place in a through-hardened martensitic AISI 52100 (100Cr6) bearing steel during RCF has been analysed using a range of characterisation and analysis methods. The results show that globular and elongated ferritic grains form during the earliest stages of the microstructure alteration in DER. The low misorientation and the occurrence of high-angle grain boundaries between the grains, and the pronounced γ -fibre texture of these components suggest that these grains are products of recrystallisation processes, possibly by dynamic recrystallisation, in the material. The stress state, at which these alterations occur can be narrowed down by the distribution of primary spheroidised carbides and retained austenite. The primary spheroidised carbides are found chemically as well as crystallographically unaltered, whereas the retained austenite has been

(a)

globular ferrite

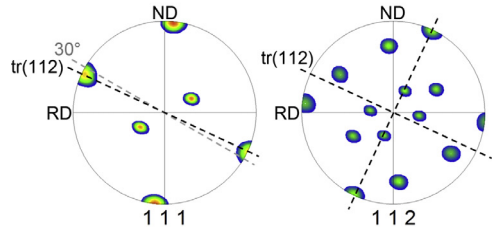
Texture Name: Harmonic; L=34, HW=2.0
Calculation Method: Harmonic Series Expansion

Series Rank (I): 34
Gaussian Smoothing: 2.0°
Sample Symmetry: Triclinic



(b)

long grains 30°



long grains 80°

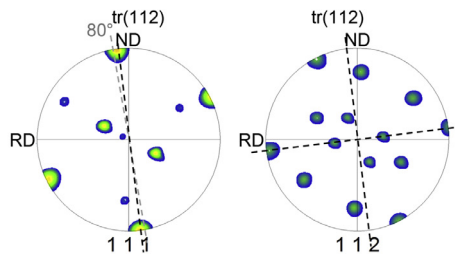


Fig. 13. Texture evaluations for the individual components: (a) RD_TD pole figures and orientation distribution function for the globular ferrite component and (b) RD-ND pole figures for the two varieties of elongated grains.

destroyed and transformed into martensite in the altered region. However, how far the austenite has been decomposed and how it is related to the subsequent alterations are still unclear since the amount of retained austenite detected in the sample was rather exceptional for typical AISI 52100 bearing microstructures.

In the combined EBSD/EDX measurements no redistribution of chemical elements was observed during the recrystallisation processes at the DER stage. However, the recrystallised structures were very small, and redistribution could have happened at scales below the spatial resolution of EDX under the given conditions. The start of globular ferritic grains recrystallisation seems to have happened slightly preferential in the chromium-depleted regions surrounded by prior spheroidised carbides.

This recrystallisation could be the starting point of a chain of microstructure alterations during RCF however it is not possible

to confirm at this stage due to the limitations of the specimens being analysed. It is possible that some martensite decay and alteration of tempered carbides have happened before the observed recrystallization but, however, was not captured. Additionally, the martensite decay and alteration of tempered carbides could have happened at a smaller scale and thus has not been observed in the SEM.

In the later stages of RCF after 30° and 80° features formed, the primary spheroidised carbides were seen to be destroyed. Globular and elongated ferritic grains were found similarly as in the DER stage but with considerably larger grain sizes, indicating that the microstructure alterations continue to grow and form ferrite crystals from DER to WEBS stage.

The EDX measurements on the WEBS have shown a clear redistribution of chemical elements. The chromium released by the

destroyed primary spheroidised carbides is compatible with the BCC lattice of the growing ferrite and has been incorporated into the newly formed crystal structures, leading to a chromium homogenisation in the altered regions, independent of the 30° or 80° orientation.

The carbon released by the carbides, however, is incompatible with the BCC lattice and is pushed out of the regions in which recrystallised ferrite grains grow. It is however not clear whether or how much elevated temperature plays a role in the recrystallisation that has affected the carbon migration. Carbon finally accumulates between the globular regions of the 30° features and close to the corners where 30° and 80° features intersect, where carbon-rich areas, possibly carbide structures, form.

The textures found for the globular ferritic grains of 30° and 80° features show a mixture of γ -fibre and rotated cube texture components, both of which are commonly found in cold rolling of BCC-iron [30].

The crystal orientation of the elongated grains is found to be uniform in each of the 30° and 80° bands, which might give an explanation of the 30° and 80° orientations of the bands. For all elongated grains, independent of the 30° or 80° orientation, a $\langle 1\ 1\ 1 \rangle$ axis lies close to the rolling normal direction. Therefore, the long grains show orientations that also occur among recrystallised globular ferritic grains. Additionally, for the elongated grains in both WEBs, a $\langle 1\ 1\ 1 \rangle$ axis lying in a {112} plane is aligned with the long shape-axis of the grains. This suggests that the elongated grains are just globular grains with a suitable orientation, which start gliding on a $\langle 1\ 1\ 1 \rangle$ {112} slip system and thus get elongated.

The asymmetric occurrence of this gliding could be a consequence of pronounced tensile forces in 30° orientation. These forces are approximately aligned with the slip system in 30° orientation and lead to the frequent and dense formation of elongated grains in the 30° features. The slip system of the elongated grains in the 80° features is affected by smaller components of these forces pointing into the direction of the slip system. Therefore, the 80° features formation takes longer and occurs less frequently. It is possibly also related to the higher temperatures in the material, which could accelerate the carbon depletion of the surrounding globular ferritic grains, leading to a stronger growth of the globular ferritic grains and larger grain sizes in the 80° features.

All the microstructure alterations discussed here were created and controlled by the rolling conditions that have led to the formation of the geometrically well-arranged features. It is noteworthy that, in the fully developed 30° and 80° features, no nanocrystalline components, similar to those found in the non-classical bearing failure due to White Etching Crack (WEC) [31,32], were observed. The differences in the microstructure alterations due to classical RCF and WEC will be detailed in another paper by the authors.

5. Conclusions

Using a combination of SEM, EBSD, EDX, TEM and nanoindentation techniques, this study has provided a detailed analysis on the microstructure alterations in a bearing steel including DER, 30° and 80° features due to classic RCF. The main conclusions from this study are:

- The primary spheroidised iron-chromium carbides $(Fe,Cr)_3C$ are found to be unaltered within the DER;
- The formation of the 30° and 80° features (WEBs) accompanies primary spheroidised carbides dissolving processes;
- In the altered microstructures of 30° and 80° features, the carbon and chromium are found to be redistributed while the pri-

mary spheroidised carbides are disintegrated and are scattered inhomogeneous and homogeneous respectively. It is thus suggested that the formation of the 30° and 80° features may be controlled by the diffusion of these chemical elements;

- The formation of globular and elongated grains is observed in both DER and WEBs however the globular and elongated grain sizes in the WEBs are much larger than those in the DER;
- The distinct directional characteristics observed in the 30° and 80° features (WEBs) may be related to the external loading conditions according to the texture analysis.

Due to the limitations on the bearing samples available to this work, the DER and WEBs were generated in ball and race specimens respectively instead of using same bearing component for all features. Further research will be conducted to confirm and compare these microstructure alterations using same component in a series of tests under controlled conditions in order to observe chronological microstructure transformation during RCF. Atom Probe Tomography (APT) will be used to examine changes in carbides and chemical elements redistribution.

Acknowledgments

Authors would like to acknowledge Basic Tribology, Competence Centre Surface Technology and Schaeffler Technologies AG & Co.KG, Germany, for providing the bearing samples and valuable suggestions to this work. We would like to extend our sincere gratitude to colleagues Kevin Kistermann, Martina Schiffers and Sebastian Zischke from GFE RWTH Aachen University for their help in sample preparation and TEM analyses. Thanks also go to Vanesa Martinez Nogues from University of Southampton for help and discussions on nanoindentation measurements.

This research has been co-funded by EPSRC (project number EP/M05062X/1) and Schaeffler Technologies, Competence Centre Surface Technology.

References

- [1] Jones AB. Metallographic observations of ball bearing fatigue phenomena. In: Proc. 49th annual meeting on 'Testing of bearings'. Buffalo, NY, USA. p. 35–52.
- [2] Muro H, Tsushima N. Microstructural, microhardness and residual stress changes due to rolling contact. Wear 1970;15:309–30.
- [3] Imai Y, Endo T, Dong D, Yamamoto Y. Study on rolling contact fatigue in hydrogen environment at a contact pressure below basic static load capacity. Tribol Trans 2010;53:764–70.
- [4] Mitamura N, Hidaka H, Takaki S. Microstructural development in bearing steel during rolling contact fatigue. Mater Sci Forum 2007;4255–60.
- [5] Osterlund R, Vingsbo O. Phase-changes in fatigued ball-bearings. Metall Trans a-Phys Metallurgy Mater Sci 1980;11:701–7.
- [6] Tricot R, Monnot J, Lluansi M. How microstructural alterations affect fatigue properties of 52100 steel. Met Eng Q 1972;12:39–47.
- [7] Martin J, Borgese S, Eberhardt A. Microstructural alterations of rolling-bearing steel undergoing cyclic stressing. J Fluids Eng 1966;88:555–65.
- [8] Borgese S. A study of the growth mechanism of lenticular carbides in cyclically stressed 52100 steel. J Tribol 1970;92:54–8.
- [9] Swahn H, Becker PC, Vingsbo O. Martensite decay during rolling-contact fatigue in ball-bearings. Metall Trans a-Phys Metall Mater Sci 1976;7:1099–110.
- [10] Scott D, Scott D. The application of electron microscopy to the study of pitting failure of rolling bearings, 1960.
- [11] Rosado L, Forster NH, Thompson KL, Cooke JW. Rolling contact fatigue life and spall propagation of AISI M50, M50nil, and AISI 52100, part I: experimental results. Tribol Trans 2009;53:29–41.
- [12] Sugino K, Miyamoto K, Nagumo M, Aoki K. Structural alterations of bearing steels under rolling contact fatigue. Trans Iron Steel Inst Jpn 1970;10:98–111.
- [13] Warhadpande A, Sadeghi F, Evans RD. Microstructural alterations in bearing steels under rolling contact fatigue part 1-historical overview. Tribol Trans May 2013;56:349–58.
- [14] O'Brien JL, King AH. Electron microscopy of stress-induced structural alterations near inclusions in bearing steels. J Fluids Eng 1966;88:568–71.
- [15] Vasilia G, Raszillier V. A study of Dark Etching Area (D.E.A.) type structure modification of material and hertzian contact area induced by ball bearing type motion. Wear 1972;19:1–15.

- [16] Voskamp A. Material response to rolling contact loading. *J Tribol* 1985;107:359–64.
- [17] Beswick J. Measurement of carbon levels in structurally transformed sae 52100 ball bearing steel by microprobe analysis. *Prakt Metallogr* 1975;12:200–6.
- [18] Bush J, Grube W, Robinson G. Microstructural and residual stress changes in hardened steel due to rolling contact. *ASM Trans* 1961;54:390–412.
- [19] Kang J. Mechanisms of microstructural damage during rolling contact fatigue of bearing steels. University of Cambridge; 2014.
- [20] Zwirlein O. Rolling contact fatigue mechanisms—accelerated testing versus field performance. In: *Rolling element bearings*, London. p. 23–7.
- [21] Schlicht H, Schreiber E, Zwirlein O. Effects of material properties on bearing steel fatigue strength. In: Effect of steel manufacturing processes on the quality of bearing steels; 1986. p. 81–101.
- [22] Bhadeshia HKDH. Steels for bearings. *Prog Mater Sci* Feb 2012;57:268–435.
- [23] Voskamp A, Österlund R, Becker P, Vingsbo O. Gradual changes in residual stress and microstructure during contact fatigue in ball bearings. *Metals Technol* 1980;7:14–21.
- [24] Polonsky IA, Keer LM. On white etching band formation in rolling bearings. *J Mech Phys Solids* 1995;43:637–69.
- [25] Beswick J, Voskamp A, Sanden Jvd, Verburgh M, Horton S. Bearing material/treatment developments at the skf engineering and research centre. In: *Creative Use of Bearing Steels*. ASTM International; 1993.
- [26] Buchwald J, Heckel RW. An analysis of microstructural changes in 52100 steel bearings during cyclic stressing. *Trans ASM* 1968;61:750–6.
- [27] Swahn H, Becker P, Vingsbo O. Electron-microscope studies of carbide decay during contact fatigue in ball bearings. *Metal Sci* 1976;10:35–9.
- [28] Muroga A, Saka H. Analysis of rolling contact fatigued microstructure using focused ion beam sputtering and transmission electron microscopy observation. *Scr Metall Mater* 1995;33:151–6.
- [29] Scott D, Loy B, Mills GH. Paper 10: metallurgical aspects of rolling contact fatigue. In: Proceedings of the institution of mechanical engineers, conference proceedings, vol. 181. 1966. p. 94–103.
- [30] Holscher M, Raabe D, Lucke K. Rolling and recrystallization textures of bcc steels. *Steel Res* 1991;62.
- [31] Diederichs AM, Schwedt A, Mayer J, Dreifert T. Electron microscopy analysis of structural changes within white etching areas. *Mater Sci Technol* 2016;32:1683–93.
- [32] Evans MH. An updated review: White Etching Cracks (WECs) and axial cracks in wind turbine gearbox bearings. *Mater Sci Technol* 2016;32:1133–69.